SIMXRD-4M: BIG SIMULATED X-RAY DIFFRACTION DATA AND CRYSTALLINE SYMMETRY CLASSIFICATION BENCHMARK

Anonymous authors
Paper under double-blind review

ABSTRACT

Powder X-ray diffraction (XRD) patterns are highly effective for crystal identification and play a pivotal role in materials discovery. While machine learning (ML) has advanced the analysis of powder XRD patterns, progress has been constrained by the limited availability of training data and established benchmarks. To address this, we introduce SimXRD, the largest open-source simulated XRD pattern dataset to date, aimed at accelerating the development of crystallographic informatics. We developed a novel XRD simulation method that incorporates comprehensive physical interactions, resulting in a high-fidelity database. SimXRD comprises 4,065,346 simulated powder XRD patterns, representing 119,569 unique crystal structures under 33 simulated conditions that reflect real-world variations. We benchmark 21 sequence models in both in-library and out-of-library scenarios and analyze the impact of class imbalance in long-tailed crystal label distributions. Remarkably, we find that: (1) current neural networks struggle with classifying low-frequency crystals, particularly in out-of-library situations; (2) models trained on SimXRD can generalize to real experimental data.

1 INTRODUCTION

Symmetry identification is a fundamental and crucial step for materials characterization and design. Specifically, Powder X-ray diffraction (XRD) analysis is exceptionally potent for probing microstructure, due to its sensitivity to atomic arrangement and the element specificity of atom scattering power. The diffraction pattern reflects the atomic arrangement of the diffracting material, as depicted in Figure 1, serving as a fingerprint of the crystals.

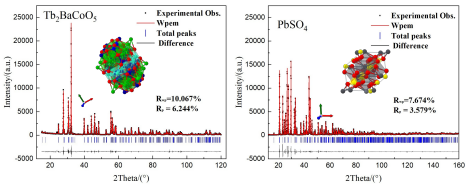

Figure 1: The X-ray diffraction patterns of crystal Tb_2BaCoO_5 and $PbSO_4$.

Traditional methods involve a search-match process (Altomare et al., 2008) among numerous known powder diffraction patterns. Given a target XRD pattern, it iterates candidates in databases until satisfactory alignment is achieved, known as search-match method. Although such a method is prevalent, it is time-consuming (Altomare et al., 2008; Lv et al., 2024; International Centre for Diffraction Data) due to two issues: (1) high dependency on human intervention. Matching processes rely on domain-specific programs that require frequent human-assisted tuning during program execution; (2) diffraction is a complex multi-physical coupling process, making structure analysis challenging even for experienced domain experts.

Inspired by the remarkable progress of machine learning models, recent studies (Lee et al., 2020; Szymanski et al., 2021; Maffettone et al., 2021; Wang et al., 2020; Salgado et al., 2023) attempt to train neural networks on simulated XRD datasets to increase the efficiency of symmetry identification. They treat XRD patterns as sequences and aim to classify them into specific crystal systems or space groups. More recent studies (Guo et al., 2024a;b; Li et al., 2024; Riesel et al., 2024; Lai et al., 2024) on powder XRD for crystal prediction and generation have employed advanced ML

architectures, achieving significant progress and noteworthy results. Despite significant progress, several limitations exist in current model development and evaluation:

- **Lack of a large-scale and high-quality dataset**: Previous research has largely confined to specific materials (Fatimah et al., 2022; Lee et al., 2020; Wang et al., 2020). For example, Lee et al. (Lee et al., 2020) focus on mixtures of 38 distinct binary and ternary crystals in the Sr-Li-Al-O inorganic compounds. Additionally, the geometric similarity of crystals and experimental physical factors can result in XRD patterns with similar peak distributions. The introduction of large-scale databases presents new challenges. Therefore, sufficient coverage of structures and close alignment with experimental patterns under different physical conditions is necessary for developing models with high generalization ability.
- **Insufficient evaluation on real XRD patterns**: While symmetry classification aims to recognize symmetry from experimental measurements, most studies train and evaluate model performance on simulated data. Considering the bias between simulated and real XRD patterns, models may overfit simulated data and fail to generalize to real data.
- **Limited exploration on out-library identification**: Most studies focus on in-library identification. This involves training a neural network to generalize across different experimental settings for the same set of crystals. In contrast, out-library identification aims to generalize to entirely new crystals. This approach is crucial for discovering novel materials but receives insufficient attention.

The limited scale of experimental data presents two significant limitations in this field: (1) insufficient data to adequately test generative capabilities, and (2) difficulty in effectively utilizing such small-scale experimental datasets for model tuning, even within a transfer learning framework, let alone for training a model solely based on experimental data. To address this dilemma, we developed high-fidelity simulation data as a solution. Our results demonstrate no observable differences in model performance between simulated and experimental test datasets, providing evidence of the high quality of the simulations. Crafting a high-fidelity simulated XRD pattern dataset is challenging due to the complexity of domain-specific processes, such as determining crystal stability, configuring instruments, and accounting for physical environmental factors. In this work, we present a novel XRD simulation method (Appendix B.4) that incorporates comprehensive physical interactions. Using this method, we developed SimXRD, the largest open-source and physically detailed dataset aimed at advancing this interdisciplinary field. We source crystals from the Materials Project (MP) (Jain et al., 2013) database and apply rigorous filtering to remove crystals with broken symmetry, duplicates, or discrepancies in space group classification. Consequently, SimXRD comprises 4,065,346 X-ray powder diffraction patterns covering 119,569 distinct crystal structures simulated under various conditions, including grain size, orientation, internal stress, inelastic scattering, thermal vibration, instrumental zero shift, and noise etc..

We benchmark both the in-library and out-library symmetry identification performance on SimXRD of 21 models, which can be divided into three types of sequence models: convolution neural networks (i.e., the backbone of existing symmetry classification models), recurrent models, and transformers. Through extensive experiments, we discover that:

- **Long-tail distribution**: The class labels follow a heavy long-tailed distribution. Most models are biased by the high-frequency classes and fail to predict the low-frequency classes, especially in space group classification. To offer insights into model designs, we evaluate the model performance under different objective functions and find that label smoothing and focal loss yield better results.
- **Out-library generalization**: Out-library classification is challenging which requires models to learn from long-tailed data and generalize to XRD patterns of unobserved crystals. Thus, the model performance of out-library classification is generally reduced compared to that of in-library classification.
- **Experimental data generalization**: Generalization ability to real experimental data is a gold standard for symmetry identification models. Remarkably, we found that models trained on the proposed SimXRD are able to achieve comparable or even better results on the real dataset, validating the contribution of our dataset construction.

We highlight that our findings can offer the research community a clearer insight into the current progress in XRD analysis. In addition, we make the SimXRD dataset, simulation code, benchmark models, evaluation process as well as tutorial notebooks into an anonymous repository: `https://anonymous.4open.science/r/SimXRDICLR`. It includes a publicly available link (of an anonymous account) to our dataset.

Table 1: Summaries of existing powder XRD datasets. ICSD refers to the commercial Inorganic Crystal Structure Database. MP denotes the open-sourced Material Project.

Dataset	#XRD Pattern	#Structure	Open Access	Simulated	Crystal Source	Year
RRUFF (Lafuente et al., 2015)	3,002	3,002	✓	×	-	2015
XRDSP (Suzuki et al., 2020)	169,536	169,536	✓	✓	**ICSD**	2020
CNN (Lee et al., 2020)	1,785,405	170	×	✓	**ICSD**	2020
PQNet (Dong et al., 2021)	250,000	1	✓	✓	**ICSD**	2021
XRDAutoAnalyzer (Szymanski et al., 2021)	38,250	150	✓	✓	**ICSD**	2021
XRDIsAllYouNeed (Lee et al., 2022)	328,503	189,476&139,027[1]	×	✓	**ICSD&MP**	2022
AdvancedXRDAnalysis (Lee et al., 2023)	29,569,650	197,131	×	✓	**ICSD**	2023
CrySTINet (Chen et al., 2024)	100	100	✓	✓	**ICSD**	2024
CPICANN (Cao, 2024)	692,190	23,073	✓	✓	**COD**	2024
SimXRD	**4,065,346**	**119,569**	✓	✓	**MP**	2024

2 Related Work

2.1 Existing datasets

Several datasets have been developed to train neural models for crystallography. Table 1 provides a summary of these datasets, compared along several key dimensions:

- **Dataset Size**: Existing open-source databases either contain relatively small structures tailored to specific purposes (Chen et al., 2024; Dong et al., 2021; Szymanski et al., 2021; Lee et al., 2020) or consider limited environmental settings (Chen et al., 2024; Suzuki et al., 2020). Crystal structure databases form the backbone of XRD pattern databases. Although the database developed by Lee et al. (Lee et al., 2022; 2023) encompasses nearly all the crystals in the Inorganic Crystal Structure Database (ICSD) (Zagorac et al., 2019) and the Materials Project (MP) (Jain et al., 2013), it contains a significant number of repeated crystals with broken symmetries. Additionally, it does not sufficiently account for various physical conditions, resulting in a relatively small XRD pattern database. SimXRD employs the entire MP database of January 2024, totaling 154,718 crystal structures. During the generation of the SimXRD database, we applied screening methods to improve crystal quality. Additionally, we simulate XRD patterns under various environments to meet the academic-industry requirements.
- **Availability**: Most pattern datasets are openly available, as indicated in Table 1, though some datasets can only be retrieved upon reasonable request (Lee et al., 2020; 2022; 2023). Additionally, published diffraction pattern datasets are saved in various formats, requiring specific data loaders provided by the authors. In contrast, the SimXRD-4M dataset developed in our work is fully available and features an easier workflow for machine learning training, easily integrable with TensorFlow or PyTorch frameworks.
- **Simulation vs. Experiments**: Among the existing datasets, only the RRUFF Project (Lafuente et al., 2015) aims to create a comprehensive set of high-quality spectral data from well-characterized minerals. Since its inception in 2005 (RRUFF, 2005), RRUFF has compiled a collection of 3,002 high-quality experimental powder XRD patterns as of March 2024. Conducting the experiments is time-consuming. Thus, recent studies have employed domain-specific software to generate simulated data. Earlier studies primarily relied on widely-used software tools, such as Pymatgen (Ong et al., 2013), FullProf (Rodríguez-Carvajal, 2001), and GSAS-II (Toby & Von Dreele, 2013), to simulate patterns for training. However, these approaches often showed varying degrees of performance drop when applied to experimental test sets. SimXRD addresses these limitations by employing the newly developed PysimXRD, which accounts for a wider range of real-world conditions. These include factors such as grain size, internal stress, external temperature variations, grain orientation, instrument drift, instrument noise, detector geometry, and

[1] Union of ICSD and MP database, existing the same structures.

scattering-induced background. This comprehensive approach ensures higher fidelity in data generation, improving the robustness of the resulting models.

2.2 SYMMETRY IDENTIFICATION

Most existing methods for symmetry identification rely on one-dimensional convolutional neural networks for building classification models. Almost all related research originates from the materials community due to the lack of easily accessible datasets. The models developed in recent years have primarily focused on CNN architectures (Dong et al., 2021; Wang et al., 2020; Park et al., 2017). In particular, they focus on designing CNNs with deep layers (Lee et al., 2022) and large kernel sizes (Le et al., 2023), ensemble CNNs (Maffettone et al., 2021; Szymanski et al., 2021), and CNNs without dropout (Lee et al., 2020) and pooling layers (Salgado et al., 2023). However, whether CNNs can address long-tailed distributions and the performance of other sequence models are still underexplored.

3 SIMXRD-4M DATASET

3.1 PRELIMINARIES

Crystal symmetry Symmetry in crystallography is a fundamental property of the orderly arrangements of atoms found in crystalline solids. Each atomic arrangement possesses certain symmetry elements, which are transformations that leave the arrangement unchanged. These elements include rotation, translation, reflection, and inversion. The specific symmetry elements present in a crystalline solid determine its shape and influence its physical properties. Crystals are classified based on their symmetry elements, falling into one of 7 *crystal systems*, and could further divide into 230 *space groups* (Clegg, 2023). Further details are provided in Appendix B.1.

XRD pattern Powder XRD patterns offer a one-dimensional representation of the three-dimensional diffraction pattern and stand as the most common experimental measurement. Specifically, each one-dimensional powder X-ray diffraction pattern in SimXRD is presented in the format of d-I (lattice plane distance-intensity), where the x-axis is lattice plane distances and the y-axis is corresponding intensities, as shown in Figure 2. The diffraction pattern we provided is a 1D tensor with 3501 elements. These points represent lattice plane distances, equally spaced from 1.199 Å to 8.853 Å, with a step size of 0.0176 Å. This corresponds to a typical experimental setup for a two-theta diffractometer (copper target), where the diffraction angle is scanned from 10° to 80° with a step size of 0.02°. The d-I pattern is independent of the wavelength of the incident X-rays, making it universally applicable across all experimental X-ray source. Lattice plane distances denote the detected atomic directions. Some distances lack peaks due to geometric constraints from the lattice cell and extinction effects (Lund et al., 2010) under diffraction. The relative intensity is normalized, with the maximum intensity value set to 100, making the pattern independent of the incident X-ray intensity.

3.2 DATA GENERATION AND PROCESSING

Crystal data The crystal structures utilized in this study were sourced from Material Project (Jain et al., 2013), a comprehensive, searchable database containing information about solid-state materials and molecules. It provides detailed data on these materials' physical properties, such as elastic tensors, band structures, and formation energies, derived from electronic structure calculations, offering a more comprehensive reference for crystal studies. We utilize the latest dataset, denoted as MP-2024.1, encompassing a total of 154,718 crystallographic structures of January 2024.

Crystal Filtering To ensure consistency between recorded space group numbers (crystal systems) and atomic arrangements, and to enhance the quality of crystal structures, we conducted a thorough examination of each structure in the MP database. We utilized Spglib (Togo et al., 2024), a library designed for identifying and managing crystal symmetries, to check all structures. Structures displaying broken symmetry, duplication, or discrepancies in space groups were excluded. Additionally, only structures containing up to 500 atoms per lattice cell were retained, effectively

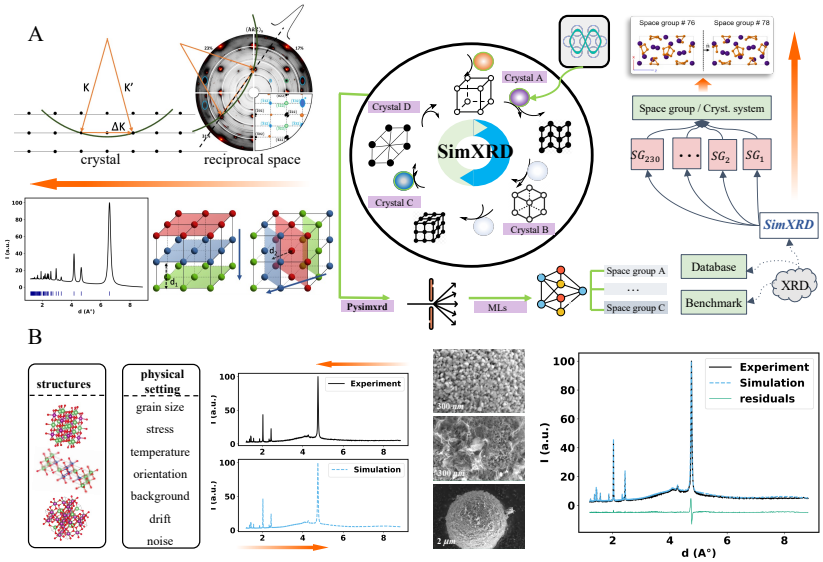

Figure 2: (A) The transformation from a crystal structure to an XRD pattern involves considerations such as finite grain size, specific orientation, thermal vibrations, zero-shift corrections, and the scattering background. The recorded patterns are represented in Q-space, with lattice distances sorted along different diffraction directions. Using the crystal database, PysimXRD generates simulated XRD patterns for ML training, enabling intelligent symmetry identification tasks. (B) We compared experimental measurement patterns with simulated XRD patterns generated using PysimXRD for a Li-rich layered oxide cathode structure, primarily composed of Li_2MnO_3. The simulation incorporates multiphysical coupling, resulting in generated patterns that align closely with experimental measurements, exhibiting small residual error.

encompassing nearly all inorganic materials in the MP dataset. A total of 119,569 crystal structures were screened. More details are given in Appendix A.1.

Simulation in SimXRD Figure 2 illustrates the overall simulation process. The experimental XRD patterns are determined by both the crystal's intricate structure and practical factors including the state of the specimen and the instrumental parameters. Our goal is to simulate this process via domain-specific custom software Pysimxrd (Appendix B.4). We first specify environmental settings and then compute the XRD patterns of given crystals. By varying the environmental parameters, we construct all samples of SimXRD. We systematically analyze the physical conditions influencing the XRD profiles, categorized into factors impacting the specimen's internal structure and those influencing instrumental measurements. These parameters, along with their respective value ranges, are introduced in the Appendix. For each input crystal, we randomly couple these physical conditions within reasonable ranges, repeating the process 33 times to simulate XRD patterns in diverse environments. Each XRD pattern is standardized, with the x-axis values (lattice plane distance) uniformly set based on the experimental settings, resulting in a vector of 3501 dimensions. The y-axis values (diffraction intensity) are simulated according to the crystal structure and diffraction conditions.

3.3 Data Analysis

Long-tailed distribution The distribution of space groups on a logarithmic scale is shown in Figure 3. The space groups in the MP dataset are ranked in descending order, and their frequencies are plotted on a logarithmic scale. This reveals differences in frequency spanning several orders of magnitude. The data clearly exhibit a highly imbalanced, long-tailed distribution. Given that MP-2024.1 serves as a comprehensive database of commonly occurring material systems, this distribution imbalance is inherent to the physical population of crystals in nature. This imbalance can lead to biased model performance as the model may be more inclined to predict the majority class, leading to lower

accuracy for the minority classes. Since minority crystal is also important for material discovery, addressing long-tailed sequence learning is crucial for symmetry identification. However, existing models do not consider such a challenge, evaluating their performance in different classes is necessary. The detailed space group distribution and the energy distribution of crystals are presented in Appendix A.1.

Case study A case study is conducted to investigate the difference between experimental and simulated XRD patterns of Li_2MnO_3. Initially, the physical states of the tested specimens and the experimental settings were obtained using a refinement method (see Appendix). Subsequently, the XRD pattern was generated inversely through the Pysimxrd. Figure 2 (B) shows their results where we can observe that the generated profile exhibits extreme similarity to the experimental measurements(Lei et al., 2024). Therefore, by altering the physical states within a reasonable range, other patterns that correspond to different experimental settings can be generated. Such simulation allows us to obtain high-quality data in a relatively efficient way, compared to experimental patterns.

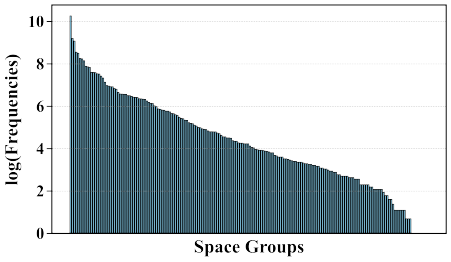

Figure 3: The distribution of space groups on logarithmic scale

4 BENCHMARK

4.1 PROBLEM DEFINITION

Symmetry classification Formally, SimXRD considers the following multi-class sequence classification problem. Given the XRD pattern $\boldsymbol{X} = [x_1, x_2, \cdots, x_n] \in \mathbb{R}^n$ where x_i is the i-th intensity value and $\boldsymbol{X}$ is arranged by lattice plane distance, the object is to predict its symmetry $\boldsymbol{Y} \in \mathbb{R}^k$. Here n is the feature dimension which is 3501 in our dataset. $k = 7$ for crystal system classification and $k = 230$ for space group classification. We did not consider practical factors such as average grain size and stress as input variables, as these are not directly measurable in real-world diffraction experiments.

In/Out-library crystallographic tasks In-library classification aims to generalize across different experimental environments for the same set of structures. Consequently, the training and testing datasets include the same structures but with varying simulation parameters. In contrast, out-library classification seeks to generalize to different crystal structures. Therefore, the training and testing datasets comprise different types of crystal structures. More details are provided in Appendix B.2.

4.2 EXPERIMENTAL SETTING

Dataset split For in-library classification, a fundamental task in crystallography, the dataset is randomly split according to the types of simulated environments, resulting in 119,569 × 30 training instances, 119,569 × 1 validation instances, and 119,569 × 2 testing instances. The data recorded for training, validation, and testing include crystals from different simulated environments (e.g., grain size, stress, temperature). Under out-of-library settings, the training and testing XRD patterns are generated from non-overlapping crystals. This setup yields 83,698 × 33 training instances, 11,957 × 33 validation instances, and 23,914 × 33 testing instances.

Baselines We consider the following three types of sequence classification models:

- **CNN-based Models**: We evaluate all existing CNN architectures that are proposed for symmetry identification. Since most of models do not have specific names, we classified them based on their number of convolution layers, pooling layers, and whether they use ensemble learning and dropout layers. Table 2 summarizes the existing 11 CNNs.
- **Recurrent Models**: We select three basic recurrent neural networks: RNN (Medsker & Jain, 1999), LSTM (Hochreiter & Schmidhuber, 1997), and GRU (Chung et al., 2014). Moreover, since

XRD patterns can be viewed from both forward and backward, we also evaluate the bidirectional RNN, LSTM, and GRU performance (Schuster & Paliwal, 1997).

- **Transformers**: Transformers have proven effective in diverse sequence modeling tasks. We evaluate the performance of raw transformer (Vaswani et al., 2017) and two advanced transformer models - iTransformer (Liu et al., 2023) and PatchTST (Nie et al., 2023).

Besides these models, we further add MLP as a straightforward baseline. For recurrent models and transformers, we first use them to learn sequence representations, and then employ an MLP to predict the symmetry.

Implementation details We use the following hyper-parameters across all experiments: Batch size 128, learning rate 2.5×10^{-4}. All models are trained for 50 epochs with an early stopping patience of 3. We use the Cross-Entropy function to measure the loss between prediction and the ground truth. We use accuracy, macro F1-score, macro precision, and macro recall as our metrics to measure the performance of the models. All models are implemented based on the Pytorch (Paszke et al., 2019) library, trained on GeForce RTX 3090 GPU.

4.3 Results

In-library classification Table 2 displays the baseline performance and inference time for the classification of crystal systems and space groups. Based on the results, we have the following observations:

- Most existing CNN models are unsuitable for symmetry identification within the large scale of the SimXRD database. It is clear that the crystal system classification accuracies of multiple CNNs, e.g., CNN 4 and 6 are on par with that of MLP. The reason, as shown in the additional results in Appendix A.2, is that their predictions are heavily biased by classes of high frequency, thus they can not predict the low-frequency classes. Such weakness is more obvious in space group classification where the accuracy of most CNNs (i.e., CNN 1-4, 6, and 8) is 0.241, indicating their outputs are almost fixed to the most frequent space group.
- Convolutional neural networks without pooling have achieved the best performance in most tasks, consistent with the findings of previous work (Salgado et al., 2023). Since the peak maximum and the relative value among peaks of XRD patterns are highly related to the atom arrangement of crystals, employing pooling layers may cause information loss, affecting the identification of peaks and leading to lower accuracy.
- Bidirectional recurrent models consistently outperform their unidirectional counterparts. These results reveal an important physical attribute of XRD patterns. That is, ensure the consistent retrieval of crystal information through bidirectional pattern reading. Such property differs from previous sequence tasks such as text and time-series classification, which requires further model designs.
- The raw transformer encounters difficulties when dealing with this long-tailed sequence problem. Nevertheless, compared to it, we can observe that PatchTST achieves significant performance improvement, demonstrating subsequence-level patches are beneficial to identify peaks and further improve classification performance.

Long-tailed objective functions The long-tailed distribution significantly impedes the symmetry identification of XRD patterns. To address this issue, we further train all baseline models using the following techniques: (1)Weighted classification that reweights training instances by the inverse of class frequency; (2) Label smoothing that applies cross-entropy with targets smoothed towards a uniform distribution; (3) Focal loss that focuses on hard-to-classify examples by down-weighting the loss for easy examples. We present the results in Table 3. The results indicate that weighted classification does not improve model performance. This lack of improvement is likely because increasing the importance of minority classes leads to a decrease in accuracy for the majority classes. In contrast, label smoothing and focal loss generally yield better results for crystal system and space group classification, providing a promising research direction for model designs.

Table 2: Results of crystal system classification and space group classification. Inference time is measured for a batch size of 100 samples and experiments are run on a GeForce RTX 3090 GPU.

Model	# Conv.	# Dropout	# Pooling	Ensemble	Ref.	Crystal System					Space Group				
						Accuracy	F1	Precision	Recall	Time (ms)	Accuracy	F1	Precision	Recall	Time (ms)
CNN1	3	✓	AvgPool	×	(Park et al., 2017)	0.559	0.418	0.427	0.431	3.2	0.241	0.002	0.001	0.005	3.4
CNN2	2	×	MaxPool	×	(Lee et al., 2020)	0.466	0.236	0.222	0.283	1.8	0.241	0.002	0.001	0.005	1.9
CNN3	3	×	MaxPool	×	(Lee et al., 2020)	0.531	0.328	0.315	0.369	3.5	0.241	0.002	0.001	0.005	3.6
CNN4	7	✓	MaxPool	×	(Wang et al., 2020)	0.316	0.069	0.045	0.143	1.4	0.241	0.002	0.001	0.005	1.4
CNN5	3	✓	AvgPool	✓	(Maffettone et al., 2021)	0.517	0.394	0.489	0.378	0.6	0.295	0.022	0.025	0.026	0.6
CNN6	7	✓	MaxPool	×	(Dong et al., 2021)	0.316	0.069	0.045	0.143	65.0	0.241	0.002	0.001	0.005	65.0
CNN7	6	✓	MaxPool	✓	(Szymanski et al., 2021)	0.862	0.863	0.887	0.845	6.8	0.588	0.124	0.147	0.130	6.9
CNN8	14	✓	MaxPool	×	(Lee et al., 2022)	0.377	0.162	0.148	0.221	3.1	0.241	0.002	0.001	0.005	3.1
CNN9	3	✓	MaxPool	×	(Le et al., 2023)	0.795	0.817	0.826	0.810	1.9	0.599	0.597	0.681	0.556	1.9
CNN10	4	✓	MaxPool	×	(Le et al., 2023)	0.870	0.888	0.892	0.885	1.8	0.705	0.792	**0.853**	0.759	1.8
CNN11	3	✓	None	×	(Salgado et al., 2023)	**0.902**	**0.922**	**0.932**	**0.914**	4.8	**0.758**	0.750	0.735	**0.828**	4.8
MLP						0.316	0.069	0.045	0.143	1.6	0.241	0.002	0.001	0.005	1.6
RNN						0.381	0.183	0.200	0.202	8.0	0.245	0.003	0.002	0.007	8.1
LSTM						0.728	0.743	0.762	0.728	14.6	0.515	0.156	0.224	0.151	14.6
GRU						0.765	0.788	0.802	0.777	15.1	0.575	0.273	0.400	0.251	15.1
Bidirectional-RNN						0.365	0.155	0.197	0.185	14.7	0.245	0.003	0.002	0.007	14.7
Bidirectional-LSTM						0.791	0.814	0.825	0.805	29.1	0.559	0.384	0.533	0.346	29.1
Bidirectional-GRU						0.800	0.826	0.840	0.816	30.3	0.627	0.451	0.609	0.408	30.3
Transformer						0.338	0.127	0.172	0.155	83.4	0.241	0.002	0.001	0.005	83.5
iTransformer						0.627	0.611	0.652	0.599	1.9	0.388	0.135	0.320	0.118	1.9
PatchTST						0.720	0.752	0.766	0.740	3.3	0.631	**0.811**	0.850	0.784	3.3

Table 3: Results of weighted classification, label smoothing, and Focal loss on crystal system and space group classification.

Crystal System Classification									
Training	**Weighted classification**			**Label smoothing**			**Focal loss**		
Metric	**F1**	**Precision**	**Recall**	**F1**	**Precision**	**Recall**	**F1**	**Precision**	**Recall**
CNN1	0.565	0.538	0.642	0.578	0.587	0.575	0.607	0.608	0.610
CNN2	0.690	0.659	0.734	0.497	0.493	0.506	0.511	0.506	0.518
CNN3	0.699	0.665	0.765	0.723	0.765	0.698	0.536	0.529	0.546
CNN4	0.229	0.191	0.390	0.066	0.043	0.142	0.066	0.043	0.142
CNN5	0.397	0.379	0.468	0.382	0.431	0.375	0.313	0.339	0.321
CNN6	0.069	0.046	0.142	0.069	0.046	0.142	0.069	0.046	0.142
CNN7	0.740	0.710	0.793	0.863	0.887	0.844	0.851	0.871	0.836
CNN8	0.546	0.533	0.625	0.566	0.590	0.559	0.554	0.687	0.547
CNN9	0.780	0.748	0.824	0.802	0.820	0.788	0.814	0.803	0.807
CNN10	0.800	0.767	**0.848**	0.877	0.898	0.860	0.844	0.857	0.834
CNN11	**0.811**	**0.797**	0.845	**0.931**	**0.943**	**0.921**	**0.887**	**0.895**	**0.882**
MLP	0.069	0.046	0.142	0.069	0.046	0.142	0.069	0.046	0.142
RNN	0.154	0.184	0.236	0.180	0.200	0.196	0.167	0.197	0.187
LSTM	0.086	0.153	0.171	0.706	0.721	0.697	0.701	0.712	0.701
GRU	0.769	0.737	0.821	0.783	0.799	0.771	0.727	0.742	0.717
Bidirectional-RNN	0.169	0.184	0.238	0.144	0.192	0.176	0.159	0.150	0.179
Bidirectional-LSTM	0.717	0.684	0.789	0.795	0.819	0.775	0.622	0.653	0.602
Bidirectional-GRU	0.704	0.674	0.777	0.861	0.863	0.863	0.845	0.843	0.847
Transformer	0.134	0.161	0.178	0.130	0.169	0.156	0.129	0.171	0.156
iTransformer	0.545	0.516	0.643	0.590	0.618	0.580	0.604	0.630	0.598
PatchTST	0.672	0.643	0.745	0.710	0.735	0.691	0.714	0.722	0.709
Space Group Classification									
CNN1	0.000	0.000	0.005	0.002	0.001	0.005	0.002	0.001	0.005
CNN2	0.000	0.000	0.005	0.002	0.001	0.005	0.002	0.001	0.005
CNN3	0.000	0.000	0.005	0.002	0.001	0.005	0.002	0.001	0.005
CNN4	0.001	0.000	0.005	0.002	0.001	0.005	0.002	0.001	0.005
CNN5	0.033	0.028	0.056	0.002	0.001	0.005	0.002	0.001	0.005
CNN6	0.000	0.001	0.005	0.002	0.001	0.005	0.002	0.001	0.005
CNN7	0.220	0.217	0.377	0.124	0.143	0.131	0.250	0.225	0.217
CNN8	0.000	0.000	0.005	0.002	0.001	0.005	0.002	0.001	0.005
CNN9	**0.391**	**0.325**	**0.739**	0.370	0.648	0.303	0.582	0.674	0.535
CNN10	0.200	0.223	0.649	0.542	0.806	0.452	**0.774**	**0.851**	0.732
CNN11	0.000	0.000	0.005	0.615	**0.836**	0.525	0.751	0.741	**0.815**
MLP	0.000	0.000	0.005	0.002	0.001	0.005	0.002	0.001	0.005
RNN	0.000	0.002	0.006	0.003	0.001	0.006	0.003	0.001	0.005
LSTM	0.000	0.000	0.006	0.143	0.210	0.137	0.140	0.206	0.137
GRU	0.215	0.180	0.610	0.185	0.261	0.176	0.227	0.192	0.653
Bidirectional-RNN	0.004	0.006	0.010	0.003	0.002	0.006	0.004	0.005	0.009
Bidirectional-LSTM	0.148	0.135	0.518	0.177	0.278	0.166	0.177	0.275	0.159
Bidirectional-GRU	0.088	0.099	0.276	0.297	0.475	0.246	0.472	0.638	0.416
Transformer	0.001	0.001	0.006	0.002	0.002	0.005	0.002	0.002	0.005
iTransformer	0.083	0.096	0.387	0.092	0.172	0.090	0.173	0.365	0.149
PatchTST	0.121	0.123	0.386	**0.677**	0.801	**0.609**	0.719	0.808	0.665

Table 4: Results of out-library symmetry identification.

Task	Crystal System Classification				Space Group Classification			
Model	Accuracy	F1	Precision	Recall	Accuracy	F1	Precision	Recall
CNN1	0.627	0.437	0.565	0.472	0.285	0.003	0.002	0.006
CNN2	0.606	0.419	0.428	0.425	0.285	0.003	0.002	0.006
CNN3	0.659	0.501	0.496	0.507	0.285	0.003	0.002	0.006
CNN4	0.378	0.078	0.054	0.142	0.285	0.003	0.002	0.006
CNN5	0.495	0.278	0.285	0.283	0.285	0.003	0.002	0.006
CNN6	0.378	0.078	0.054	0.142	0.285	0.003	0.002	0.006
CNN7	0.673	0.607	0.633	0.608	0.429	0.053	0.050	0.072
CNN8	0.612	0.452	0.448	0.497	0.286	0.003	0.001	0.006
CNN9	0.675	0.632	0.629	0.644	0.439	0.099	0.137	0.113
CNN10	0.692	0.659	0.650	0.674	0.430	0.107	0.168	0.121
CNN11	0.702	0.672	0.659	0.690	0.481	0.136	0.167	**0.150**
MLP	0.378	0.078	0.054	0.142	0.285	0.003	0.002	0.006
RNN	0.409	0.162	0.149	0.178	0.274	0.003	0.002	0.009
LSTM	0.657	0.575	0.583	0.589	0.431	0.070	0.092	0.085
GRU	0.707	0.678	0.656	**0.709**	0.480	0.110	0.143	0.125
Bidirectional-RNN	0.403	0.157	0.146	0.174	0.295	0.004	0.003	0.008
Bidirectional-LSTM	0.704	0.663	0.654	0.678	0.349	0.035	0.044	0.051
Bidirectional-GRU	**0.722**	**0.699**	**0.697**	0.705	**0.498**	**0.138**	**0.192**	0.149
Transformer	0.376	0.138	0.231	0.158	0.285	0.003	0.005	0.006
iTransformer	0.606	0.495	0.519	0.526	0.367	0.053	0.085	0.064
PatchTST	0.656	0.616	0.612	0.627	0.375	0.067	0.093	0.082

Out-library classification Different splitting mechanisms are essential for preliminary experiments. Consequently, we perform experiments using out-of-library settings, where the training and testing XRD patterns originate from non-overlapping structures. We randomly partition the dataset by crystal type to ensure that the training, validation, and test datasets are composed of distinct crystals. The results are detailed in Table 4. Based on the results, we have the following observations:

- Performance decrease compared to in-library classification. This decline is anticipated, as out-of-library classification requires models to generalize across diverse crystal types, presenting a greater challenge.
- The relative model performances is consistent with the results from in-library identification, with Bidirectional-GRU and CNN11 achieving higher scores. However, there is a noticeable decline in performance for out-of-library cases, as the models need to account for varying extinction effects across different space groups, which poses significant challenges.
- Most models, such as CNN1-4, CNN6, CNN8, MLP, and Transformer, exhibit poor performance in out-of-library identification, with accuracy scores around 24%, close to random prediction. This highlights the need for further development of domain-specific models to effectively address out-of-library identification challenges.

Experimental data generalization A generalization experiment is conducted using the experimental RRUFF dataset. We train and validate all baseline models on SimXRD and then test their performance on RRUFF. The results are presented in Table 5. The results show that the models generally achieve consistent performance on both SimXRD and RRUFF. Notably, CNN 11 continues to deliver the best accuracy, even surpassing its performance on SimXRD (e.g., CNN 11 in space group classification). Models with lower accuracy on SimXRD (e.g., CNN 1-6) also perform poorly on RRUFF.

5 CONCLUSION

In this paper, we propose SimXRD, the largest open-source XRD pattern dataset for symmetry identification. The data analysis reveals that the symmetry labels follow a long-tailed distribution. We evaluate 21 models on two different splitting patterns (in-library and out-of-library) and find that most existing models struggle to accurately predict the symmetry of low-frequency classes, even when accounting for class imbalance. This limitation affects their real-world applicability. Our results underline the importance of modeling long-tailed sequence classification and comprehensive comparison in accurately understanding the capabilities of various models. We make SimXRD

Table 5: Generalization experiments on RRUFF dataset.

Task	Crystal System Classification				Space Group Classification			
Model	**Accuracy**	**F1**	**Precision**	**Recall**	**Accuracy**	**F1**	**Precision**	**Recall**
CNN1	0.623	0.542	0.563	0.539	0.241	0.004	0.002	0.010
CNN2	0.425	0.210	0.178	0.143	0.241	0.004	0.002	0.010
CNN3	0.506	0.313	0.397	0.332	0.241	0.004	0.002	0.010
CNN4	0.297	0.065	0.042	0.143	0.241	0.004	0.002	0.010
CNN5	0.530	0.402	0.511	0.384	0.302	0.043	0.045	0.051
CNN6	0.297	0.065	0.042	0.143	0.241	0.004	0.002	0.010
CNN7	0.868	0.877	0.899	0.860	0.577	0.202	0.205	0.222
CNN8	0.297	0.065	0.042	0.143	0.241	0.004	0.002	0.010
CNN9	0.792	0.819	0.832	0.809	0.615	0.500	0.555	0.486
CNN10	0.859	0.885	0.893	0.879	0.696	0.685	0.741	0.669
CNN11	**0.893**	**0.920**	**0.930**	**0.914**	**0.766**	**0.700**	**0.754**	**0.687**
MLP	0.325	0.070	0.046	0.143	0.241	0.004	0.002	0.010
RNN	0.377	0.165	0.203	0.185	0.245	0.006	0.004	0.013
LSTM	0.723	0.735	0.747	0.731	0.522	0.230	0.275	0.230
GRU	0.774	0.801	0.817	0.788	0.575	0.360	0.421	0.357
Bidirectional-RNN	0.365	0.152	0.190	0.184	0.245	0.005	0.003	0.013
Bidirectional- LSTM	0.788	0.813	0.820	0.808	0.553	0.367	0.419	0.354
Bidirectional-GRU	0.804	0.845	0.864	0.834	0.636	0.448	0.512	0.429
Transformer	0.354	0.138	0.219	0.165	0.241	0.004	0.002	0.010
iTransformer	0.629	0.612	0.658	0.607	0.392	0.143	0.156	0.151
PatchTST	0.723	0.764	0.785	0.750	0.635	0.696	0.748	**0.687**

and the simulation code open-source to facilitate further research and improvement of symmetry identification algorithms.

Limitations Although SimXRD enhances prior datasets from multiple perspectives (e.g., sample size, crystal quality, and accessibility), long-tailed and imbalanced label distribution is its inherent limitation. The distribution of crystallographic symmetry arises through natural processes and is invariant to human intervention. Such biases are difficult to address in any dataset. Thus, possible solutions are to develop specific class-imbalanced algorithms or employ additional information on target crystals.

Future works We view SimXRD as an evolving project and are committed to its ongoing development. Future plans include: (1) Developing long-tailed sequence classification models through techniques such as data augmentation (Chu et al., 2020) or enhancing features via multi-modal inputs; (2)Deriving training approaches, such as multi-stage learning, to address the imbalanced nature of XRD patterns; (3) Designing data augmentation strategies for XRD patterns, while ensuring that methods like random swapping do not generate instances that violate underlying physical principles.

REFERENCES

Angela Altomare, Corrado Cuocci, Carmelo Giacovazzo, Anna Moliterni, and Rosanna Rizzi. Qualx: a computer program for qualitative analysis using powder diffraction data. *Journal of Applied Crystallography*, 41(4):815–817, 2008.

BH Armstrong. Spectrum line profiles: the voigt function. *Journal of Quantitative Spectroscopy and Radiative Transfer*, 7(1):61–88, 1967.

G Caglioti, AT Paoletti, and FP Ricci. Choice of collimators for a crystal spectrometer for neutron diffraction. *Nuclear Instruments*, 3(4):223–228, 1958.

Bin Cao. Cpicann. `https://huggingface.co/datasets/caobin/datasetCPICANN`, 2024. Accessed: 2024-05-21.

Litao Chen, Bingxu Wang, Wentao Zhang, Shisheng Zheng, Zhefeng Chen, Mingzheng Zhang, Cheng Dong, Feng Pan, and Shunning Li. Crystal structure assignment for unknown compounds from x-ray diffraction patterns with deep learning. *Journal of the American Chemical Society*, 146(12):8098–8109, 2024.

Peng Chu, Xiao Bian, Shaopeng Liu, and Haibin Ling. Feature space augmentation for long-tailed data. In *ECCV*, volume 12374, pp. 694–710, 2020.

Junyoung Chung, Caglar Gulcehre, KyungHyun Cho, and Yoshua Bengio. Empirical evaluation of gated recurrent neural networks on sequence modeling. *arXiv preprint arXiv:1412.3555*, 2014.

William Clegg. Space groups–the final frontier: a tutorial guided tour of some entries in international tables for crystallography volume a. *Crystallography Reviews*, 29(4):228–246, 2023.

Hongyang Dong, Keith T Butler, Dorota Matras, Stephen WT Price, Yaroslav Odarchenko, Rahul Khatry, Andrew Thompson, Vesna Middelkoop, Simon DM Jacques, Andrew M Beale, et al. A deep convolutional neural network for real-time full profile analysis of big powder diffraction data. *NPJ Computational Materials*, 7(1):74, 2021.

Siti Fatimah, Risti Ragadhita, Dwi Fitria Al Husaeni, and Asep Bayu Dani Nandiyanto. How to calculate crystallite size from x-ray diffraction (xrd) using scherrer method. *ASEAN Journal of Science and Engineering*, 2(1):65–76, 2022.

Gabe Guo, Judah Goldfeder, Ling Lan, Aniv Ray, Albert Hanming Yang, Boyuan Chen, Simon JL Billinge, and Hod Lipson. Towards end-to-end structure determination from x-ray diffraction data using deep learning. *npj Computational Materials*, 10(1):209, 2024a.

Gabe Guo, Tristan Saidi, Maxwell Terban, Simon JL Billinge, and Hod Lipson. Diffusion models are promising for ab initio structure solutions from nanocrystalline powder diffraction data. *arXiv preprint arXiv:2406.10796*, 2024b.

Sepp Hochreiter and Jürgen Schmidhuber. Long short-term memory. *Neural computation*, 9(8): 1735–1780, 1997.

JH Hubbell, WH McMaster, N Kerr Del Grande, and JH Mallett. International tables for x-ray crystallography. *Vol. IV*, pp. 45–70, 1974.

International Centre for Diffraction Data. Mdi jade software. `https://www.icdd.com/mdi-jade/`. Accessed: 2024-05-18.

Anubhav Jain, Shyue Ping Ong, Geoffroy Hautier, Wei Chen, William Davidson Richards, Stephen Dacek, Shreyas Cholia, Dan Gunter, David Skinner, Gerbrand Ceder, et al. Commentary: The materials project: A materials genome approach to accelerating materials innovation. *APL materials*, 1(1), 2013.

Barbara Lafuente, Robert T Downs, Hexiong Yang, Nate Stone, Thomas Armbruster, Rosa Micaela Danisi, et al. The power of databases: the rruff project. *Highlights in mineralogical crystallography*, 1:25, 2015.

Qingsi Lai, Lin Yao, Zhifeng Gao, Siyuan Liu, Hongshuai Wang, Shuqi Lu, Di He, Liwei Wang, Cheng Wang, and Guolin Ke. End-to-end crystal structure prediction from powder x-ray diffraction. *arXiv preprint arXiv:2401.03862*, 2024.

Nam Q Le, Michael Pekala, Alexander New, Edwin B Gienger, Christine Chung, Timothy J Montalbano, Elizabeth A Pogue, Janna Domenico, and Christopher D Stiles. Deep learning models to identify common phases across material systems from x-ray diffraction. *The Journal of Physical Chemistry C*, 127(44):21758–21767, 2023.

Armel Le Bail. Whole powder pattern decomposition methods and applications: A retrospection. *Powder diffraction*, 20(4):316–326, 2005.

Armel Le Bail, Huguette Duroy, and Jean Louis Fourquet. Ab-initio structure determination of lisbwo6 by x-ray powder diffraction. *Materials Research Bulletin*, 23(3):447–452, 1988.

Byung Do Lee, Jin-Woong Lee, Woon Bae Park, Joonseo Park, Min-Young Cho, Satendra Pal Singh, Myoungho Pyo, and Kee-Sun Sohn. Powder x-ray diffraction pattern is all you need for machine-learning-based symmetry identification and property prediction. *Advanced Intelligent Systems*, 4 (7):2200042, 2022.

Byung Do Lee, Jin-Woong Lee, Junuk Ahn, Seonghwan Kim, Woon Bae Park, and Kee-Sun Sohn. A deep learning approach to powder x-ray diffraction pattern analysis: Addressing generalizability and perturbation issues simultaneously. *Advanced Intelligent Systems*, 5(9):2300140, 2023.

Jin-Woong Lee, Woon Bae Park, Jin Hee Lee, Satendra Pal Singh, and Kee-Sun Sohn. A deep-learning technique for phase identification in multiphase inorganic compounds using synthetic xrd powder patterns. *Nature communications*, 11(1):86, 2020.

Tongxing Lei, Bin Cao, Wenbo Fu, Xiuling Shi, Zhiyu Ding, Qi Zhang, Junwei Wu, Kaikai Li, and Tong-Yi Zhang. A li-rich layered oxide cathode with remarkable capacity and prolonged cycle life. *Chemical Engineering Journal*, pp. 151522, 2024.

Qi Li, Rui Jiao, Liming Wu, Tiannian Zhu, Wenbing Huang, Shifeng Jin, Yang Liu, Hongming Weng, and Xiaolong Chen. Powder diffraction crystal structure determination using generative models. *arXiv preprint arXiv:2409.04727*, 2024.

Yong Liu, Tengge Hu, Haoran Zhang, Haixu Wu, Shiyu Wang, Lintao Ma, and Mingsheng Long. itransformer: Inverted transformers are effective for time series forecasting. *CoRR*, abs/2310.06625, 2023.

Kristina Lund, Norihiro Muroyama, and Osamu Terasaki. Accidental extinction in powder xrd intensity of porous crystals: Mesoporous carbon crystal cmk-5 and layered zeolite-nanosheets. *Microporous and mesoporous materials*, 128(1-3):71–77, 2010.

Luca Lutterotti, Henry Pilliere, Christophe Fontugne, Philippe Boullay, and Daniel Chateigner. Full-profile search–match by the rietveld method. *Journal of applied crystallography*, 52(3):587–598, 2019.

Binfeng Lv, Zhenjie Feng, Xiaowei Sun, Jian Cao, Yu Gao, Shihui Chang, Cheng Dong, and Jincang Zhang. iqual: a new computer program for qualitative phase analysis with efficient search–match capability. *Journal of Applied Crystallography*, 57(2), 2024.

Phillip M Maffettone, Lars Banko, Peng Cui, Yury Lysogorskiy, Marc A Little, Daniel Olds, Alfred Ludwig, and Andrew I Cooper. Crystallography companion agent for high-throughput materials discovery. *Nature Computational Science*, 1(4):290–297, 2021.

K Maniammal, G Madhu, and V Biju. X-ray diffraction line profile analysis of nanostructured nickel oxide: Shape factor and convolution of crystallite size and microstrain contributions. *Physica E: Low-dimensional Systems and Nanostructures*, 85:214–222, 2017.

Larry Medsker and Lakhmi C Jain. *Recurrent neural networks: design and applications*. 1999.

RP Millane. R factors in x-ray fiber diffraction. ii. largest likely r factors. *Acta Crystallographica Section A: Foundations of Crystallography*, 45(8):573–576, 1989.

MAR Miranda and JM Sasaki. The limit of application of the scherrer equation. *Acta Crystallographica Section A: Foundations and Advances*, 74(1):54–65, 2018.

Yuqi Nie, Nam H. Nguyen, Phanwadee Sinthong, and Jayant Kalagnanam. A time series is worth 64 words: Long-term forecasting with transformers. In *ICLR*, 2023.

Shyue Ping Ong, William Davidson Richards, Anubhav Jain, Geoffroy Hautier, Michael Kocher, Shreyas Cholia, Dan Gunter, Vincent L Chevrier, Kristin A Persson, and Gerbrand Ceder. Python materials genomics (pymatgen): A robust, open-source python library for materials analysis. *Computational Materials Science*, 68:314–319, 2013.

Woon Bae Park, Jiyong Chung, Jaeyoung Jung, Keemin Sohn, Satendra Pal Singh, Myoungho Pyo, Namsoo Shin, and K-S Sohn. Classification of crystal structure using a convolutional neural network. *IUCrJ*, 4(4):486–494, 2017.

Adam Paszke, Sam Gross, Francisco Massa, Adam Lerer, James Bradbury, Gregory Chanan, Trevor Killeen, Zeming Lin, Natalia Gimelshein, Luca Antiga, et al. Pytorch: An imperative style, high-performance deep learning library. *Advances in neural information processing systems*, 32, 2019.

GS Pawley. Unit-cell refinement from powder diffraction scans. *Journal of Applied Crystallography*, 14(6):357–361, 1981.

Eric A Riesel, Tsach Mackey, Hamed Nilforoshan, Minkai Xu, Catherine K Badding, Alison B Altman, Jure Leskovec, and Danna E Freedman. Crystal structure determination from powder diffraction patterns with generative machine learning. *Journal of the American Chemical Society*, 146(44):30340–30348, 2024.

HM Rietveld. Line profiles of neutron powder-diffraction peaks for structure refinement. *Acta Crystallographica*, 22(1):151–152, 1967.

Hugo M Rietveld. A profile refinement method for nuclear and magnetic structures. *Journal of applied Crystallography*, 2(2):65–71, 1969.

Juan Rodríguez-Carvajal. An introduction to the program fullprof 2000. *Version July*, 54, 2001.

Mario Enrique Rodriguez-Garcia, Martin Adelaido Hernandez-Landaverde, Jose Miguel Delgado, Cristian Felipe Ramirez-Gutierrez, Marius Ramirez-Cardona, Beatriz M Millan-Malo, and Sandra Milena Londoño-Restrepo. Crystalline structures of the main components of starch. *Current Opinion in Food Science*, 37:107–111, 2021.

RRUFF. Rruff, 2005. URL `https://gsa.confex.com/gsa/2005AM/webprogram/Paper92745.html`. Accessed: 2024-05-21.

Jerardo E Salgado, Samuel Lerman, Zhaotong Du, Chenliang Xu, and Niaz Abdolrahim. Automated classification of big x-ray diffraction data using deep learning models. *npj Computational Materials*, 9(1):214, 2023.

Mike Schuster and Kuldip K Paliwal. Bidirectional recurrent neural networks. *IEEE transactions on Signal Processing*, 45(11):2673–2681, 1997.

Yuta Suzuki, Hideitsu Hino, Takafumi Hawai, Kotaro Saito, Masato Kotsugi, and Kanta Ono. Symmetry prediction and knowledge discovery from x-ray diffraction patterns using an interpretable machine learning approach. *Scientific reports*, 10(1):21790, 2020.

EC Svensson, VF Sears, ADB Woods, and P Martel. Neutron-diffraction study of the static structure factor and pair correlations in liquid he 4. *Physical Review B*, 21(8):3638, 1980.

Nathan J Szymanski, Christopher J Bartel, Yan Zeng, Qingsong Tu, and Gerbrand Ceder. Probabilistic deep learning approach to automate the interpretation of multi-phase diffraction spectra. *Chemistry of Materials*, 33(11):4204–4215, 2021.

Brian H Toby. R factors in rietveld analysis: How good is good enough? *Powder diffraction*, 21(1): 67–70, 2006.

Brian H Toby and Robert B Von Dreele. Gsas-ii: the genesis of a modern open-source all purpose crystallography software package. *Journal of Applied Crystallography*, 46(2):544–549, 2013.

Atsushi Togo, Kohei Shinohara, and Isao Tanaka. `Spglib`: a software library for crystal symmetry search, 2024.

David Turnbull. Phase changes. In *Solid state physics*, volume 3, pp. 225–306. 1956.

University College London. X-ray powder diffraction quality assurance tables, date accessed. URL `http://pd.chem.ucl.ac.uk/pxrd/qa/smtable.htm`.

B Van Laar and WB Yelon. The peak in neutron powder diffraction. *Journal of Applied crystallography*, 17(2):47–54, 1984.

Ashish Vaswani, Noam Shazeer, Niki Parmar, Jakob Uszkoreit, Llion Jones, Aidan N. Gomez, Lukasz Kaiser, and Illia Polosukhin. In *Neurips*, pp. 5998–6008, 2017.

Hong Wang, Yunchao Xie, Dawei Li, Heng Deng, Yunxin Zhao, Ming Xin, and Jian Lin. Rapid identification of x-ray diffraction patterns based on very limited data by interpretable convolutional neural networks. *Journal of chemical information and modeling*, 60(4):2004–2011, 2020.

Dejan Zagorac, H Müller, S Ruehl, J Zagorac, and Silke Rehme. Recent developments in the inorganic crystal structure database: theoretical crystal structure data and related features. *Journal of applied crystallography*, 52(5):918–925, 2019.

A ADDITIONAL RESULTS

A.1 LONG-TAILED DISTRIBUTION AND FORMATION ENERGY

The distributions of space groups and crystal systems are shown in Figure 4A and B. The formation energy (E_f) of a configuration represents the energy required or released to generate that configuration. Thus, the formation process can be either endothermic or exothermic. The more negative the formation energy of a structure, the more stable the structure, indicating its thermal stability Turnbull (1956). Figures 4C and D illustrate the formation energy per atom across 154,718 crystal structures in MP-2024.1 and 119,569 crystal structures in SimXRD. Figure 4C highlights the high-quality crystal data in MP-2024.1, with 90.33% of structures exhibiting negative formation energy. Sequentially, the crystal data in SimXRD shows a negative formation energy rate of 92.18%, indicating that the excluded crystals are mainly relatively unstable structures. This high-quality structural data serves as the cornerstone of XRD pattern databases.

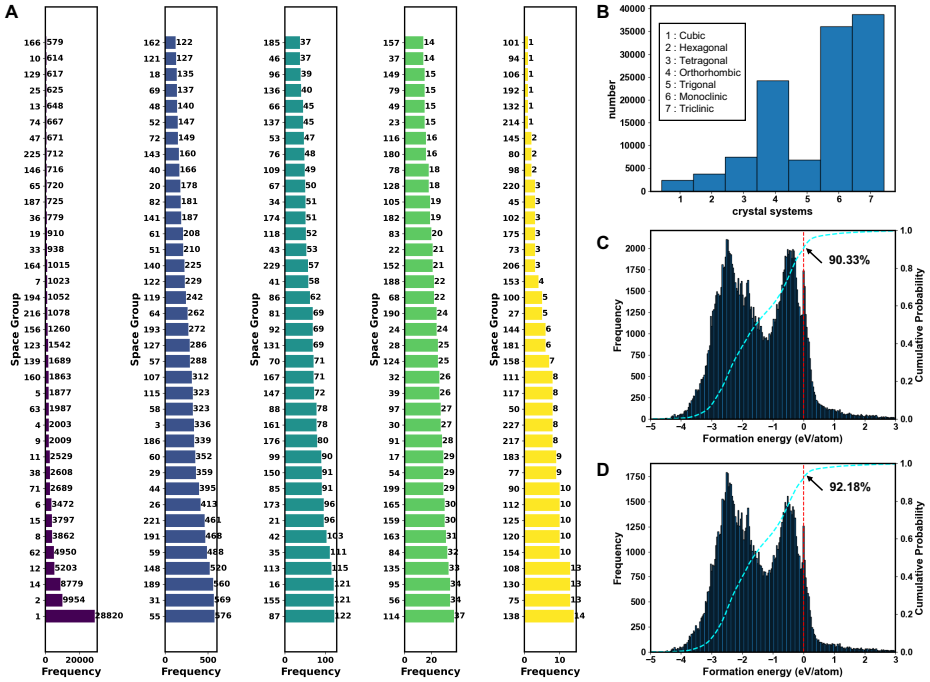

Figure 4: The statics of dataset. (A) The distribution of structures contained in the SimXRD database across various space groups (uniformly divided into 5 categories according to the frequency) and (B) crystal systems (C) The distribution of –formation energy/atom of crystals contained in MP-2024.1 and (D) SimXRD. Space groups 89, 103, and 104 have been excluded from Figure A to enhance clarity, each appearing only once.

A.2 PERFORMANCE W.R.T. LONG-TAILED DISTRIBUTION

To further investigate the model performance, we display the accuracy of each crystal system and space group of different frequencies in Figure 5 under in-library symmetry identification. To better visualize the model performance on space group, we divided the results of 280 space groups into 5 categories according to their frequency (the same as Figure 4). From the results, we can observe:

- In crystal system classification, the performance of most CNN models, the raw RNN, and transformers is affected by the frequency of crystal systems. They can not predict the XRD patterns of Cubic and Hexagonal symmetry (their accuracies are almost zero). In contrast, multiple domain-specific CNN (i.e., CNN 7, 9, 10, 11), LSTM, GRU, and advanced Transformers (i.e., iTransformer and PatchTST) can mitigate long-tail distributions.

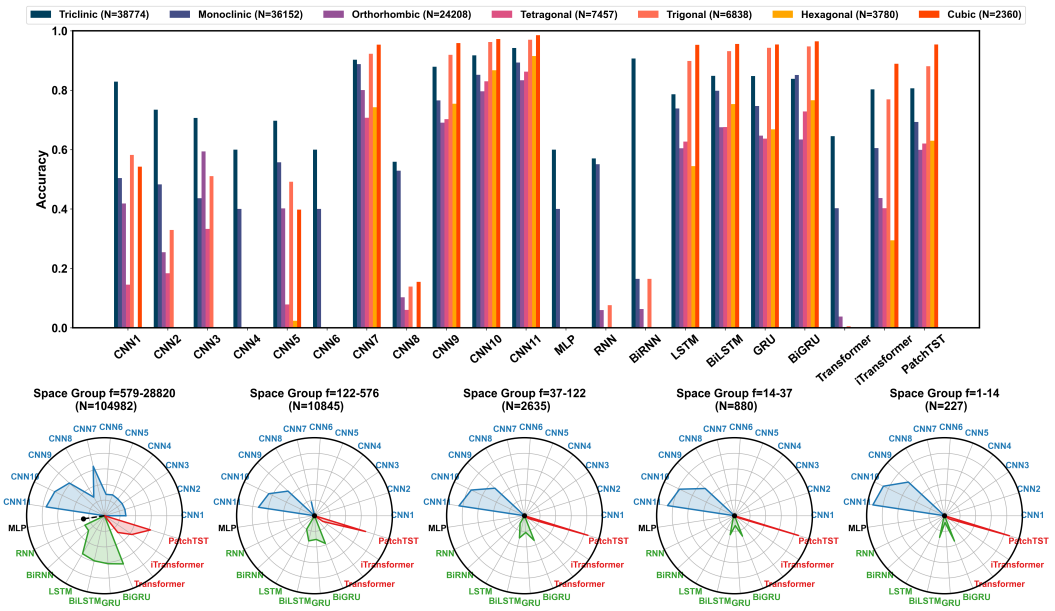

Figure 5: Classification accuracy of each model w.r.t. crystal systems and space groups. The same as Figure 4(A), Space groups are classified into 5 categories based on their frequency. N denotes the number of crystals.

- Space group classification is more challenging than crystal system classification. Most models can only predict space groups with high frequency and hardly predict most low-frequency space groups. Surprisingly, PatchTST achieves comparable performance with the best models in all low-frequency space groups. Given that PatchTST is a model specifically tailored for time series forecasting, its performance on XRD pattern classification has considerable room for improvement.

A.3 Feature Analysis

We also analyze the relative feature importance map to provide model interpretability. By masking features in powder XRD patterns, we observe the impact of the masked features on the model's inference by calculating the relative accuracy drop. This approach reflects the relative importance of the masked features for model classification. As expected, masking critical features results in a significant drop in accuracy.

To further investigate, we categorize peak features into five groups based on their intensity: (1) Peaks with intensities within the 0–20% maximum intensity interval, (2) Peaks within the 20–40% intensity interval, (3) Peaks within the 40–60% intensity interval, (4) Peaks within the 60–80% intensity interval, and (5) Peaks within the 80–100% intensity interval. We evaluate the model's inference performance with these masked features, as shown in Figure 6. The results demonstrate a clear trend: when high-intensity peaks, particularly those in category 5, are masked, a significant accuracy drop is observed across all baselines. This indicates that the ML model heavily relies on high-intensity peaks, similar to the "characteristic peaks" identified in search-match approaches.

Interestingly, for models that perform well on relative tasks, masking peaks in categories 3 or 4 also noticeably affects performance. This suggests that these models capture more comprehensive pattern characteristics by giving attention to relatively weak intensity peaks. Such behavior is reasonable for deep neural networks, as they extract more detailed information rather than relying solely on the '3 strongest diffraction peaks'. This leads to better performance compared to traditional search-match techniques.

Comparing the results of CNN11, BiGRU, and PatchTST, three models that performed relatively well in these symmetry identification tasks, we observe distinct strategies for decision-making. CNN11 places greater emphasis on characteristic peaks in category 5, indicating that its inference approach aligns closely with the traditional search-match method, though it considers more peaks than the "three strongest diffraction peaks" typically used in search-match. PatchTST follows a similar trend, but the relative accuracy drop is more pronounced, suggesting that PatchTST captures a broader range of peak characteristics compared to CNN11. In contrast, BiGRU exhibits a gradient in the accuracy drop, indicating that it selectively focuses on relatively strong peaks while progressively reducing emphasis on weaker peaks based on their intensity. This approach is intuitively reasonable, as weaker peaks are more susceptible to noise. These observations suggest that bidirectional architectures, such as BiGRU, may provide a promising solution for studying powder XRD data, as concluded in the main text.

B Additional Background

B.1 More details about crystal symmetry

The seven crystal systems are cubic(#1), hexagonal(#2), tetragonal(#3), orthorhombic(#4), trigonal(#5), monoclinic(#6), and triclinic(#7) system. Crystals can be diagrammatically represented by an orderly stacking of lattice cells, whose shape determines the crystal system to which they belong. Unit cells of identical shape can have lattice points, representing an atom or group of atoms, at their centers or faces, in addition to the corners. These additional lattice points further divide the seven crystal systems into 14 Bravais lattices, which are then subdivided into 32 crystal classes, or point groups. Each point group corresponds to a possible combination of rotations, reflections, inversions, and improper rotations. When translational elements are included, these point groups yield the 230 space groups (Clegg, 2023).

B.2 In-library and Out-of-library Tasks

In-library identification is a fundamental task in crystallography that aims to accurately identify crystal types based on XRD patterns measured in various environments. Since 1938, crystallographers have been documenting all discovered structures and archiving them as Powder Diffraction Files (PDFs) . By comparing and retrieving these PDFs, researchers can determine the structures of studied materials by matching them with historical data. With advancements in computing, numerous software programs have been developed to assist in the search-match process.

A related concept is out-of-library identification, which involves discovering previously unknown structures that lack any recorded information. This process relies on symmetry identification to determine the basic space group information and subsequent refinement processes. Traditionally, the crystal system to which a crystal belongs can be determined based on the crystal's physical properties, such as electrical conductivity, optical behavior, and thermal characteristics. Subsequently, the space group can be identified by examining extinction effects . This is followed by determining the ideal chemical formula according to the estimated number of atoms and Wyckoff positions . Validation is conducted through Rietveld refinement and site optimization, among other techniques.

Therefore, we provided two types of splits:

- **In-library Classification:** In our in-library benchmark, the dataset is divided based on different simulation environments. Both the training and testing datasets contain the same structures, but under varying simulation conditions. This setup corresponds to in-library identification in XRD phase analysis.
- **Out-of-library Classification:** In our out-of-library benchmark, the dataset is split according to crystal types. The training and testing datasets consist of different structures, mirroring the out-of-library identification process in XRD phase analysis.

B.3 Search-Match approach

Conventionally, the predominant method for in-library phase identification in X-ray powder diffraction patterns is the search-match approach, which comprises three main steps. Initially, (d, I) values,

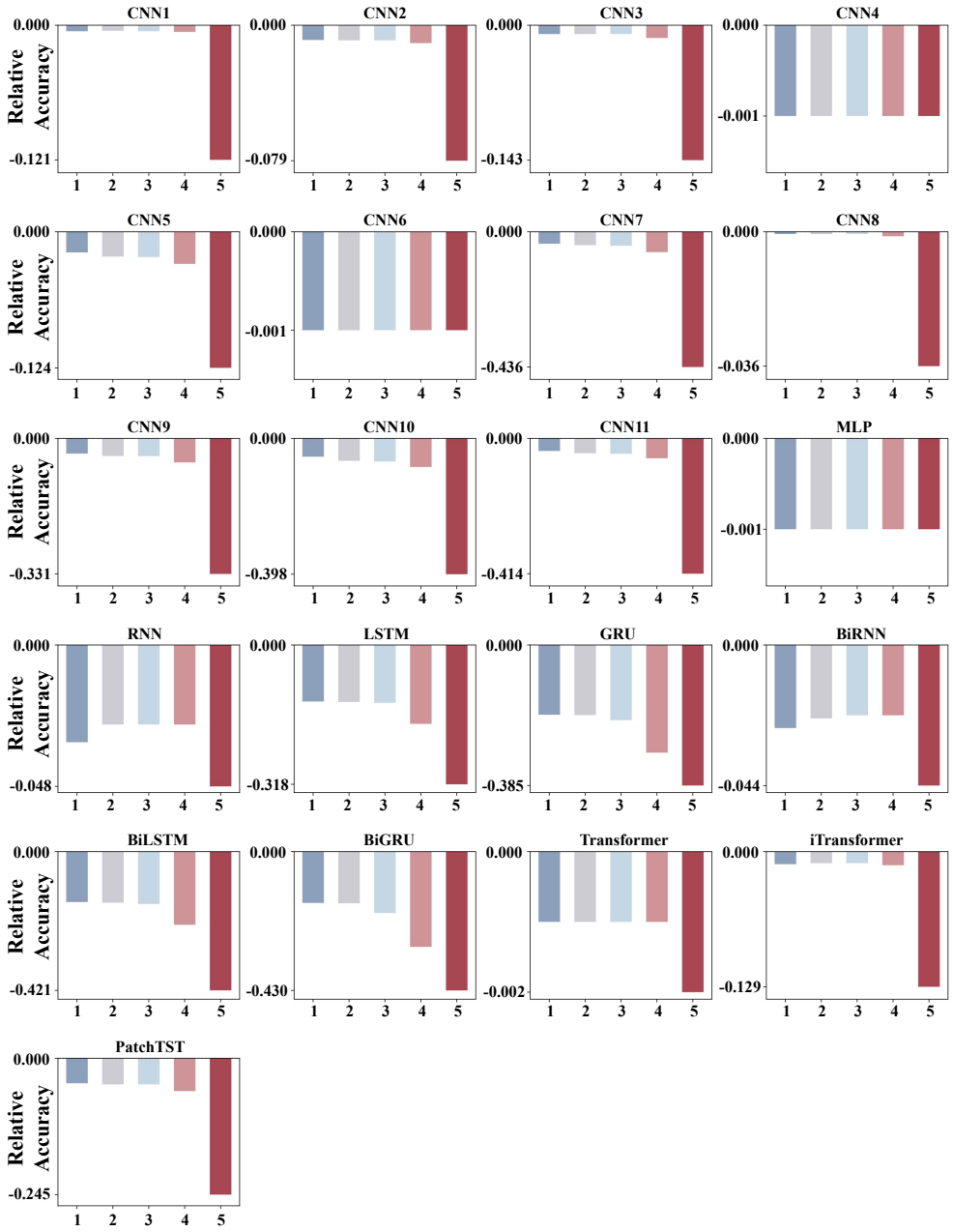

Figure 6: The relative classification accuracy drops when peak features are masked across all baselines. These features are categorized into five groups based on their intensity. 1: Peaks with intensities within the 0–20% maximum intensity interval, 2: Peaks within the 20–40% intensity interval, 3: Peaks within the 40–60% intensity interval, 4: Peaks within the 60–80% intensity interval, and 5: Peaks within the 80–100% intensity interval.

representing interplanar spacing (d) and intensity (I) of each peak, are extracted from the pattern. Subsequently, potential phases are sought from diffraction databases based on characteristic d values, such as Hanawalt indexes (University College London, date accessed). Following this, candidate phases are compared to the (d, I) values of the pattern using a scoring system to assess alignment, aiding in selecting the most suitable candidate phase. This process iterates until satisfactory

alignment is achieved for most (d, I) values. A recent study (Lutterotti et al., 2019) employs a distinct approach utilizing the Rietveld method for conducting a Full Profile Search-Match (FPSM). Crystal structures selected from databases are automatically aligned with raw data via the Rietveld method, culminating in a score determined by R_{wp} (Millane, 1989). The phase with the highest score is acknowledged, and this iterative procedure persists until specified criteria are met. Subsequently, a Rietveld quantification is executed to ascertain the weight fraction of each phase. Despite advancements in computer technology enabling novel qualitative analysis methods, the core workflow of search-match remains consistent: to match experimental data with database entries and calculate a corresponding score.

B.4 XRD Pattern Simulation

Powder XRD provides a one-dimensional representation of three-dimensional diffraction patterns and is the most common experimental measurement, as shown in Figure 8. These patterns reflect the relative arrangement of atoms in three-dimensional space. The interaction of X-rays with condensed materials during diffraction involves elastic collisions between photons and electrons. Consequently, factors affecting atomic arrangement and electron behavior influence the shape of the diffraction pattern, highlighting the pressing need for developing high-fidelity simulation technologies. To address this gap, we developed Pysimxrd.

The diffraction vector $\mathbf{G}^*$ is defined as

$$|\mathbf{G}^*| = \frac{2\sin\theta}{\lambda}, \tag{1}$$

where λ is the wavelength of the scattered particle and $\theta = 2\theta/2$, with 2θ being the angle between the incident and diffracted beams. In three dimensions, scattering occurs only at a discrete set of reciprocal vectors, $\mathbf{K}$, forming the reciprocal lattice,

$$\mathbf{K} = h\mathbf{a}^* + k\mathbf{b}^* + l\mathbf{c}^*, \tag{2}$$

where $\mathbf{a}^*$, $\mathbf{b}^*$, and $\mathbf{c}^*$ are the reciprocal lattice vectors, and h, k, and l are constants. The diffraction condition is defined as

$$2\pi\mathbf{G}^* = \mathbf{K}. \tag{3}$$

The x-axis of simulation patterns d is the reciprocal of $|\mathbf{G}^*|$, i.e., $d = 1/|\mathbf{G}^*|$.

The diffraction intensity I on each diffraction vector $\mathbf{G}^*$ for a single phase is determined by

$$I(\mathbf{G}^*) = SF^*F\varnothing LPOD + I^{\mathrm{BG}}, \tag{4}$$

where S denotes the scale factor, F is the structure factor, F^* is the complex conjugate of F, $\varnothing$ is the profile function, L is the Lorentz-polarization factor, P is the multiplicity, O is the preferred orientation factor, D is the Debye-Waller factor, and I^{BG} is the background intensity. The structure factor is computed as:

$$F = \sum_{j=1}^{N} f_j e^{2\pi i \mathbf{G}^* \cdot \mathbf{R}}, \tag{5}$$

where f_j is the form factor Hubbell et al. (1974) in XRD, $\mathbf{R}$ is the lattice coordinate of atom j, and N is the total number of atoms in a lattice cell.

The Lorentz-polarization L is calculated by,

$$L = \frac{1 + \cos^2 2\theta}{\sin^2\theta\cos\theta}. \tag{6}$$

where $\theta = \arcsin\left(\frac{\lambda|\mathbf{G}^*|}{2}\right)$. The multiplicity P is determined by counting the number of diffraction vectors present within an Ewald diffraction sphere. The Debye-Waller factor D is calculated by ,

$$D = e^{-2M}, \tag{7}$$

where $M = \frac{6h^2T}{mk\Theta^2}\left(\phi\left(\frac{\Theta}{T}\right) + \frac{\Theta}{4T}\right)\left(\sin^2\theta\right)/\lambda$, h is Planck's constant, m is atom mass, k is Boltzmann constant, Θ is the average characteristic temperature, T is absolute temperature, and $\phi(\Theta/T)$ is the Debye function.

The profile function ($\varnothing$) is modeled by convolving various factors, including diffraction, detector geometry, and noise factors etc. The simulated peaks are calculated by:

$$y(x) = W * G * S \tag{8}$$

Here, * denotes the convolution process, and W, G, and S represent the contributions to the observed XRD pattern from diffraction emission, instrumental factors, and the noise mixture, respectively. S is modeled as a Gaussian peak.

The W is a Voigt function Armstrong (1967),

$$W = \frac{1}{\sigma\sqrt{2\pi}} \int_{-\infty}^{\infty} \left[\frac{\gamma}{(2\theta - t)^2 + \gamma^2} \right] \exp\left(-\frac{(2\theta - t)^2}{2\sigma^2} \right) dt, \tag{9}$$

Peak broadening is correlated with the Full Width at Half Maximum (FWHM, Γ), where $2\gamma = 2\sqrt{2\ln 2}\sigma = \Gamma$ Caglioti et al. (1958). Γ is calculated by Scherrer's equation Miranda & Sasaki (2018) related to finite grain size.

The geometrical factorVan Laar & Yelon (1984), G, accounts for the actual dimensions of the detectors and the powder specimen. It is defined as follows:

$$D(2\alpha, 2\theta) = \frac{\delta I(2\theta)}{\delta(2\alpha)} d(2\alpha) \tag{10}$$

$$G(2\alpha, 2\theta) = \frac{L}{4HSh\cos(2\alpha)} \int dz \tag{11}$$

where 2α represents the Bragg angle. The detector is slit-shaped, with a height of $2H$, and the sample has a height of $2S$. L denotes the distance between the specimen and the detector.

The simulation environments in our study encompass three key aspects. The first aspect pertains to the specimen, where we simulate the average grain size, the ideal orientation effect of the powder, and the lattice cell's extinction and torsional deformation under internal stress. The second aspect involves the testing conditions, accounting for factors such as atomic thermal vibrations at room temperature, air scattering-induced signal noise, and instrumental vibration-induced noise. The third aspect relates to the diffractometer, including the zero shift of the angular position and detector's geometry.

The adjustable parameters of the simulation environments include:

- Finite grain size (for Voigt peaks): the average grain size is set as a random number in the range of 2 nm to 50 nm to replicate the degree of experimental broadening (Maniammal et al., 2017) (If a convolution peak is applied, the range needs to be adjusted accordingly). Instrumental broadening becomes apparent in the experimental patterns as convolution with the crystal peak occurs. Typically, in the refinement process, it is common to separate observed peaks into Voigt and instrumental components. However, quantifying the instrumental component proves challenging as it varies with the diffraction angle. Therefore, in our simulations, we opt for a smaller grain size than realistic to accurately replicate the degree of experimental broadening.
- Orientation: the ideal powder specimen is assumed to have no orientation, however, this is impossible. The orientation effect arises from the uneven distribution of small grains in the incident beam, leading to an uneven distribution of reciprocal sites across the reciprocal spheres of the powder specimen. To simulate the impact of orientation, we set the intensity by perturbation within a 40% range based on the ideal simulation to mimic the orientation randomness.
- Thermal vibration: the temperature is converted to the kinetic energy of atoms, which is simulated by allowing atoms to shift from their average positions within a range of 0.01-0.5 angstrom.
- Internal stress: internal stress is simulated by applying elastic deformation of the recorded lattice constant by up to 10%.
- Instrument zero shifting: the zero shift is simulated by randomly translating 2θ within -1.2 to 1.2 degrees.

- Instrument noise: 2% Gaussian white noise is added to the entire pattern to reflect instrument noise.
- Inelastic Scattering: A sixth-order polynomial function is employed to simulate the background distribution, encompassing phenomena such as Compton scattering, fluorescence, and multiple scattering. This simulated background is then integrated into the XRD pattern with a 2% ratio.

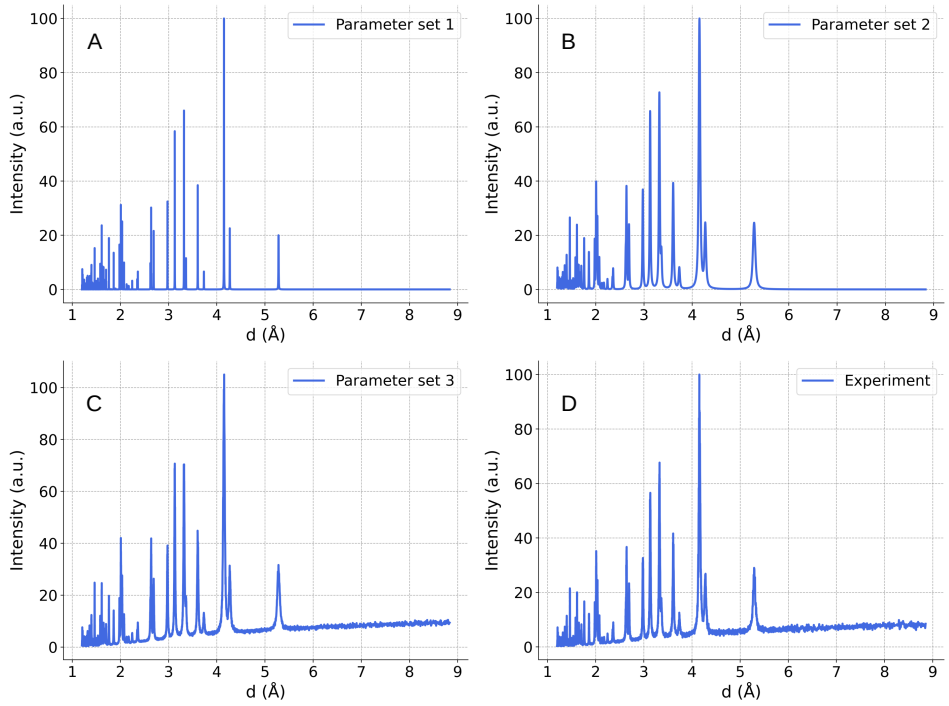

Figure 7: Comparison of simulation pattern with experimental pattern of $PbSO_4$ (A) The generated $PbSO_4$ powder XRD without considering the simulation environment. (B) The generated $PbSO_4$ powder XRD based on a set of parameters that account for finite grain size, orientation, thermal vibrations, and internal stress. (C) The generated $PbSO_4$ powder XRD with an extended set of parameters that further include zero-shift correction, noise, peak convolution, and background effects. (D) The experimentally observed data. Note: The $PbSO_4$ structure corresponds to entry 1010950.cif from the Crystallography Open Database. The parameter sets used in the simulations were optimized by minimizing the differences between the simulated and experimental patterns, rather than being randomly assigned. All patterns were converted to Q-space using a wavelength of 1.54 Å.

As illustrated in Figure 7, the multiphysical coupling observed in experimental XRD can be incorporated into the simulation parameter space by introducing more realistic conditions. Specifically, considering factors such as orientation, thermal vibrations, zero-shift corrections, noise, and other sources of randomness significantly improves the realism of the simulations. These parameters collectively influence the arrangement of peaks, their intensities, and overall shapes in the diffraction pattern.

B.5 Crystal and Diffraction

Among various investigative methods, diffraction analysis stands out as exceptionally potent for probing microstructure, primarily due to its sensitivity to atomic arrangement and the element specificity of atom scattering power. Each intensity maximum, termed a line profile or peak, within a diffraction pattern reflects the atomic arrangement along certain direction of the diffracting material.

Powder X-ray diffraction, in particular, furnishes a remarkably diverse array of structural details, encoded in the material- and instrument-specific distribution of coherently scattered monochromatic wave intensity, with wavelengths corresponding to lattice spacing. The X-rays are generated by a

cathode ray tube, filtered to produce monochromatic radiation, collimated for concentration, and directed towards the sample. When conditions satisfy Bragg's Law, which relates the wavelength of electromagnetic radiation to the diffraction angle and lattice spacing in a crystalline sample, the incident rays interact with the sample to produce constructive interference and a diffracted ray, as shown in Figure 8.

The diffracted X-rays are subsequently detected, processed, and quantified. By scanning the sample across a range of diffraction angles, all possible diffraction directions of the lattice are accessible due to the random orientation of powdered material.

B.6 Symmetry recognition in structure determination

Pattern refinement (Rietveld, 1967; 1969) is essential for accurately determining the crystal structure in diffraction practices. In XRD refinement, the critical initial step involves identifying the crystalline phase of the given pattern. This phase identification is crucial as it facilitates the calculation of the static structure factor (Svensson et al., 1980), which aids in determining atom sites during refinement. The primary step in refinement is establishing the geometry of the crystal lattice cell by solving the diffraction indices corresponding to a set of lattice planes for each diffraction peak, a process known as indexing calculation (Rodriguez-Garcia et al., 2021).

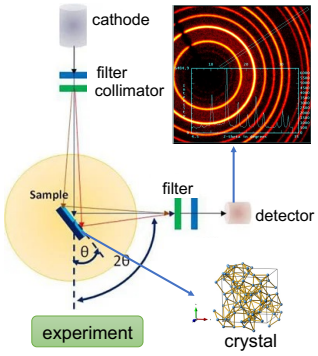

Figure 8: Experimental procedure for recording XRD patterns.

Utilizing existing crystal databases, the commonly employed search-match approach retrieves potential structures that match the observed pattern, essentially performing in-library identification. The matched structure, along with basic crystallographic information, including crystal symmetry, serves as a foundational element for further analysis.

Whether the observed patterns are from in-library or out-of-library crystals, symmetry identification combined with indexing is a generic method for determining lattice geometry to initiate the refinement process. This is why many researchers in materials science and physics pursue a general method to derive the symmetry of structures based on diffraction patterns. Once the fundamental crystallographic information is acquired, techniques such as pattern decomposition and Rietveld refinement (Rietveld, 1967; 1969; Le Bail, 2005) come into play. These methodologies facilitate the determination of atom sites, temperature factors, grain sizes, residual stress, and other intricate structural details from the diffraction patterns on a case-by-case basis, thereby contributing to the comprehensive elucidation of a crystal structure.

B.7 Whole Powder Pattern Fitting and Refinement

Structure refinement is an effective method for determining crystal structures. Traditionally, refinement begins with a set of reasonably estimated parameters with physical significance. Accurately identifying the structure's space group aids in establishing rational parameters. However, without prior structural knowledge, this process becomes trial and error. Although identifying the space group initiates the process, its validation relies on refinement outcomes.

A significant advancement in powder diffraction fitting for structure refinement emerged with the Rietveld method(Rietveld, 1967; 1969), which pioneered whole pattern fitting over the analysis of individual, non-overlapping Bragg diffraction peaks. The Whole Powder Pattern Fitting (WPPF) approach within the Rietveld method uses profile intensity calculations and a least-squares algorithm for structure refinement. By minimizing the disparities between observed experimental profiles and theoretical profiles, it extracts all structural information. Once fitting reaches its limit, the parameters in the theoretical model represent the only determinable physical information. SimXRD's pattern simulation also relies on the structural information contained within the theoretical model. The Pawley(Pawley, 1981) and Le Bail(Le Bail et al., 1988) methods, two widely used WPPF techniques, are developed after the Rietveld method.

Table 6: Parameter Categories comparison of crystal systems & space group

Task	Crystal System Classification			Space Group Classification		
Metric	Category1	Category2	Category3	Category1	Category2	Category3
CNN1	0.523	0.553	0.554	0.250	0.233	0.241
CNN2	0.452	0.467	0.464	0.250	0.233	0.241
CNN3	0.318	0.384	0.307	0.250	0.233	0.241
CNN4	0.375	0.305	0.302	0.250	0.233	0.241
CNN5	0.500	0.545	0.526	0.312	0.286	0.295
CNN6	0.375	0.305	0.302	0.250	0.233	0.241
CNN7	0.781	0.894	0.862	0.437	0.566	0.575
CNN8	0.375	0.305	0.302	0.250	0.233	0.241
CNN9	0.781	0.823	0.785	0.343	0.646	0.609
CNN10	**0.812**	**0.908**	0.868	0.406	0.727	0.704
CNN11	0.656	**0.908**	**0.895**	**0.562**	**0.823**	**0.775**
MLP	0.312	0.327	0.324	0.250	0.233	0.241
RNN	0.468	0.383	0.367	0.218	0.236	0.245
LSTM	0.593	0.761	0.727	0.281	0.577	0.515
GRU	0.531	0.793	0.765	0.437	0.596	0.575
Bidirectional-RNN	0.343	0.362	0.365	0.250	0.236	0.245
Bidirectional-LSTM	0.781	0.837	0.790	0.437	0.600	0.559
Bidirectional-GRU	0.656	0.818	0.800	0.437	0.596	0.575
Transformer	0.375	0.364	0.338	0.250	0.233	0.240
iTransformer	0.500	0.662	0.627	0.312	0.378	0.388
PatchTST	0.562	0.745	0.720	0.437	0.672	0.631

These parameters with physical significance are diverse, and one important type is peak shape parameters. The parameters of each diffraction peak (positions, intensities, and shapes) within a whole XRD pattern offer detailed structural insights from different aspects, making their quantitative and accurate extraction from the overall XRD profile highly significant. This quantification of peak information and the subsequent derivation of physical parameters constitute the essence of the refinement endeavor.

B.8 Parameters intervals study

To study how simulation parameters influence model performance on SimXRD, we perform an additional comparison by dividing the testing instances into three distinct intervals based on their key simulation parameters:

- **Category 1:** Grain size (nm) $\in [2, 10]$, atomic thermal offset (Å) $\in [0.4, 0.5]$, orientation randomness (%) $\in [30, 40]$, zero shifting (°) $\in [1, 1.2]$.
- **Category 2:** Grain size (nm) $\in [40, 50]$, atomic thermal offset (Å) $\in [0, 0.1]$, orientation randomness (%) $\in [0, 10]$, zero shifting (°) $\in [0, 0.2]$.
- **Category 3:** The parameter domain excludes Category 1 and Category 2.

The three parameter categories represent three simulated experimental scenarios: Category 1 reflects a high degree of peak broadening and external influence, while Category 2 is aligned with relative ideal conditions, exhibiting lower broadening and noise. Category 3 represents an intermediate state between the two. The accuracy of space group classification is displayed in Table 6. The results indicate that the baselines generally perform better in Category 2 and exhibit the lowest accuracy in Category 1, underscoring the challenges of modeling experimental XRD patterns in more complex physical situations. These insights highlight the need for developing a high-fidelity database that encompasses diverse crystals and covers a sufficient range of practical scenarios.

B.9 Sim2Real Gap

To illustrate the advantages of Pysimxrd in generating high-fidelity powder XRD patterns, we compared its performance with a widely recognized software, GSAS-II (Toby & Von Dreele, 2013). The simulation process involves the use of refinement software, starting with the determination of suitable parameter sets through the refinement procedure provided by each software. The lattice constants derived from these refinements are summarized in Table 7. Once the parameters are confirmed, the corresponding simulation patterns are generated.

Table 7: Derived crystal structures in refinement.

		Lattice Constants (Å)					
Models	**Crystals**	**a**	**b**	**c**	α	β	γ
Pysimxrd	Mn_2O_3	9.4082(2)	9.4082(2)	9.4082(2)	90	90	90
Pysimxrd	RuO_2	4.5381(7)	4.5381(7)	3.1248(4)	90	90	90
GSAS-II	Mn_2O_3	9.4197(1)	9.4197(1)	9.4197(1)	90	90	90
GSAS-II	RuO_2	4.5351(8)	4.5351(8)	3.1226(0)	90	90	90

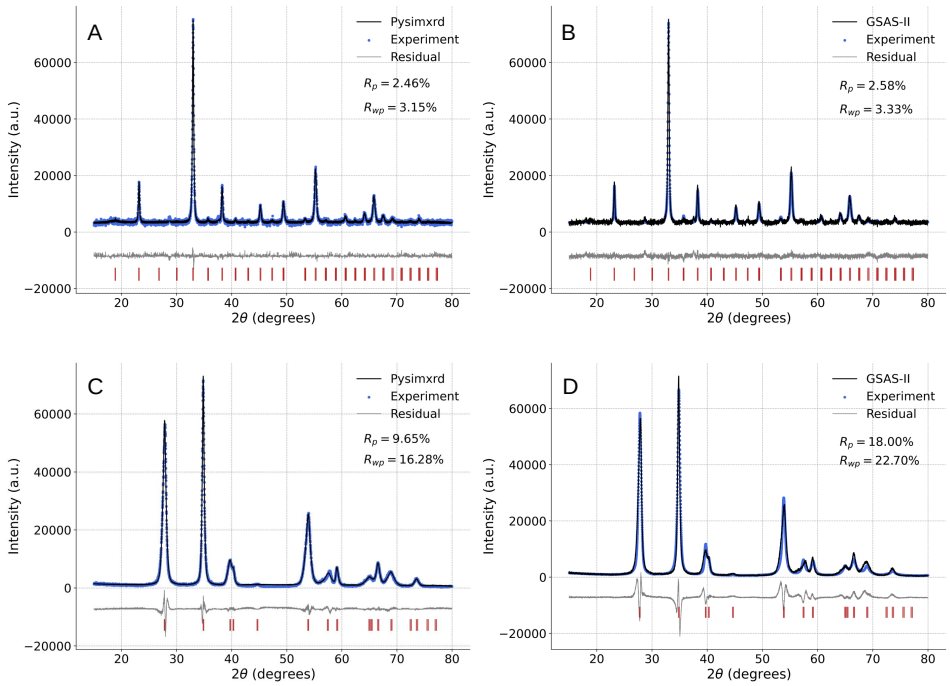

Figure 9: Comparison of simulated and experimental patterns: (A) The Mn_2O_3 pattern simulated using Pysimxrd. (B) The Mn_2O_3 pattern simulated using GSAS-II. (C) The RuO_2 pattern simulated using Pysimxrd. (D) The RuO_2 pattern simulated using GSAS-II. The R-factors, calculated as (Toby, 2006), are used to evaluate the quality of the fitting.

Two experimental powder XRD patterns were obtained using an X'Pert Pro MPD (Panalytical) in Bragg-Brentano geometry with a copper X-ray source ($\lambda_{\text{K-}\alpha} = 1.5406$ Å). The samples used were Mn_2O_3 and RuO_2 crystals. As shown in Figure 9, Pysimxrd and GSAS-II demonstrated comparable accuracy in reconstructing the Mn_2O_3 pattern. However, Pysimxrd showed significant advantages in reconstructing the RuO_2 pattern. This superiority stems from Pysimxrd's ability to account for a broader range of simulation environments and its greater flexibility in tuning parameters, which resulted in a more accurate reconstruction with lower R-factors.